

Article

# The Design of a Contactless Unregulated Power Converter for the Separated Modules

Yan Zhou , Yu Sun and Ziwen Yang

Department of Electrical Engineering, College of Automation, Nanjing University of Posts and Telecommunications, Nanjing 210023, China; 1218053511@njupt.edu.cn (Y.S.); B17050416@njupt.edu.cn (Z.Y.)

\* Correspondence: zhouyan@njupt.edu.cn; Tel.: +86-138-1386-3836

Received: 28 June 2020; Accepted: 4 August 2020; Published: 9 August 2020



**Abstract:** In the contactless unregulated power converter application with high output current, optimizing coil structures and using synchronous rectification are important for achieving high efficiency. This paper proposes a separated planar structure of coils to achieve the design goals and gives its equivalent circuit model. On the power transmitting pad, double coils are used to enhance the ability of the output power levels. In order to implement full-wave synchronous rectification (FWSR), the power receiving pad also adopts double coils. The power coils on both sides have similar structures to obtain a balance-induced voltage in each half of the switching period, and the principles of the optimal turn ratio in coils are discussed. Meanwhile, four typical self-driven coil structures are compared and analyzed. The effect of the coupling coefficient and load currents on the loss of the duty cycle is discussed. To satisfy the requirements of output voltage, the rules for selecting the minimum ferrite core are summarized. A 120 W unregulated intermediate bus converter is built. The whole system achieves 90.7% efficiency under all loading ranges, and the maximum efficiency of the system is 94.5% at a 3.5A load current.

**Keywords:** contactless unregulated power converter; coils design; separated modular structure

## 1. Introduction

In recent years, electronic systems are designed as isolated modular structures to enhance the flexibility or the productivity of the system [1–5]. For example, the famous Bluefin-21, which is an autonomous undersea vehicle, is 5 m long nearly, as shown in Figure 1a. The traditional solution uses a central battery to offer power for the whole system, so the long wires are used to provide power for different point of loads. However, this design has some inherent drawbacks. First, manufacturing such a long electronic system may need several months. Based on the functional modular design structures, the system can be built in a few weeks and is easy to install. Second, the whole system may become invalid when some components are not working properly, and the system comprised with separated modules can be maintained easily. However, an additional power battery may be needed in each separated module and will weigh the system obviously. Therefore, the contactless power supply can offer the power for different separated modules and better waterproofing properties, as shown in Figure 1b.

Inductive power transfer realizes energy transmission through the air to support a contactless design. The literature [6,7] introduces the principles of coupling mechanism design, control strategy, and stability in the system of inductive power transfer. Due to a relative low coupling coefficient between two coils in a contactless transformer, traditional solutions suffered low voltage gain and low efficiency. Especially when the system needs large output currents, the loss of duty cycle caused by leakage inductance will reduce the amplitude of output voltages further. The authors of [8] used a method of impedance response to achieve the desired power output curve over a wide range of load

resistance. In order to form a relatively uniform magnetic field to improve their efficiency, optimal coil structures have been widely investigated, such as coil array [9,10], single spiral coil structure [11], and hybrid coil structure [12]. Using LC (inductor-capacitor network) compensation networks to form a resonant tank in circuits can greatly enhance the voltage gain and transmission power, but the voltage in the receiving side is too high to use for a point-of-load (POL) application directly. Additional stepdown power converters are needed, and this will increase the volume and cost [13].

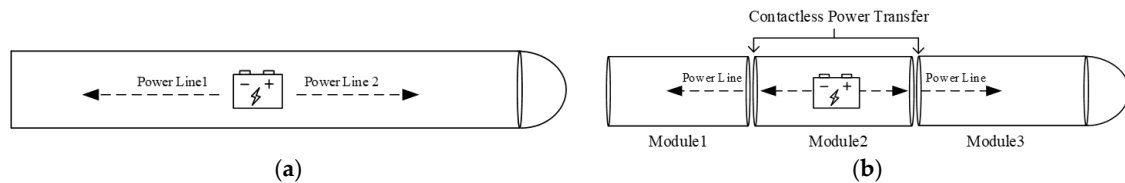


**Figure 1.** Architectures of the power supply for long electric systems. (a) Traditional solution. (b) Contactless solution for the modular design.

There are mainly two rectifier methods to transfer AC voltage to DC voltage, as shown in Figure 2. For the center-tapped rectifier, two diodes are connected to the center-tapped secondary winding of the transformer in Figure 2a. D1 and D2 work in every half of the AC cycle, respectively. When one diode is forward-biased, another diode is reverse-biased and suffers two times the inverse voltage. Therefore, a center-tapped rectifier is usually used in the application of the low output voltage. Bridge rectifiers have four diodes to provide full-wave rectification, as shown in Figure 2b. D1 and D3 or D2 and D4 conduct during every half-cycle of the AC cycle, respectively, so two diodes always conduct in circuits and result in a larger voltage drop than only one diode involved in center-tapped rectifier. However, the inverse voltage of diodes in the bridge rectifier is only half of that in the center-tapped rectifier. As a result, the bridge rectifier is used for high-voltage applications, normally. In this paper, we needed to design a wireless power converter with the low output voltage and large output current, so we needed to design the double coils to form the center-tapped rectifier in the receiver side. In order to generate the balanced induction voltage during every half of the AC cycle in the double coils, we also needed to investigate the arrangement of the double coils in the transfer side. At the same time, we use the skills of a synchronous rectifier to replace the diodes to enhance the efficiency further. There are two main methods to generate a gate drive signal for synchronous rectification: self-driven signal and external-driven signal. The driving signal from an external IC (integrated circuit) can ensure the reliable operation of the rectification. However, this solution is hard to apply for a contactless power transfer with an air gap [14]. The other method is using a self-driven synchronous rectification. For a slow dynamic response speed, detecting the drain-source voltage of the rectifier to generate drive signals is not suitable for high-frequency applications [15]. An auxiliary coil is used to detect the working polarity to generate self-driven signals in the secondary side [16–23]. However, this low-cost solution is only discussed in tightly coupled transformers. In a loosely coupled system, how to achieve the stability of the self-driven signals has not been clearly researched.

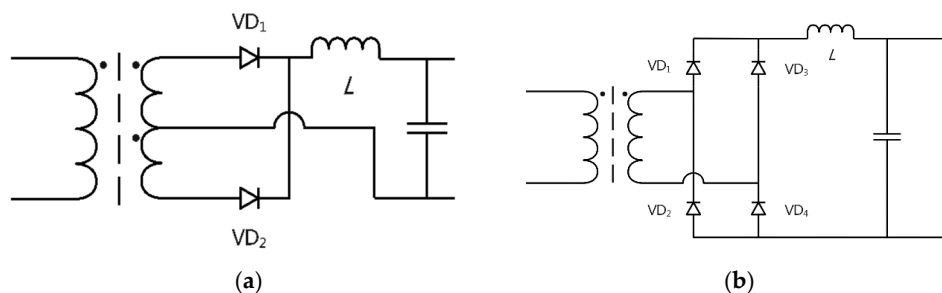


**Figure 2.** The main rectifier methods. (a) Center-tapped rectifier. (b) Bridge rectifier.

This paper proposes a structure for a contactless power converter with self-driven synchronous rectification. Double coils are used in both sides to improve the coupling coefficient, so the efficiency and voltage gain of the system are improved greatly. The optimal method for the inner and outer coils on the pad is investigated to generate a symmetrically induced voltage. Furthermore, four typical arrangements of self-driven coils are compared to get a suitable drive signal.

## 2. System Structure and Equivalent Model

### 2.1. Operating Principle

The main circuit of the contactless bus converter is shown in Figure 3a. A full-bridge inverter is used to generate a high-frequency AC voltage  $U_{AB}$ , and the double transmitting coils  $L_1$  and  $L_2$  are connected in parallel. In a contactless power transfer system, a low coupling coefficient will result in a large leakage inductance,  $L_s$ . In order to achieve self-driven synchronous rectification, the receiving coils  $L_3$  and  $L_4$  are connected with a central-tapped structure. The driving coil  $L_d$  is used to provide the driving signals for synchronous rectifier,  $Q_5$  and  $Q_6$ . The filter consists of  $L_o$  and  $C_o$ , and the load is represented by  $R_{load}$ .  $Q_1$  to  $Q_6$  are MOSFET(metal-oxide-semiconductor field-effect transistor) switches, and  $D_1$  to  $D_6$  are Schottky diodes.

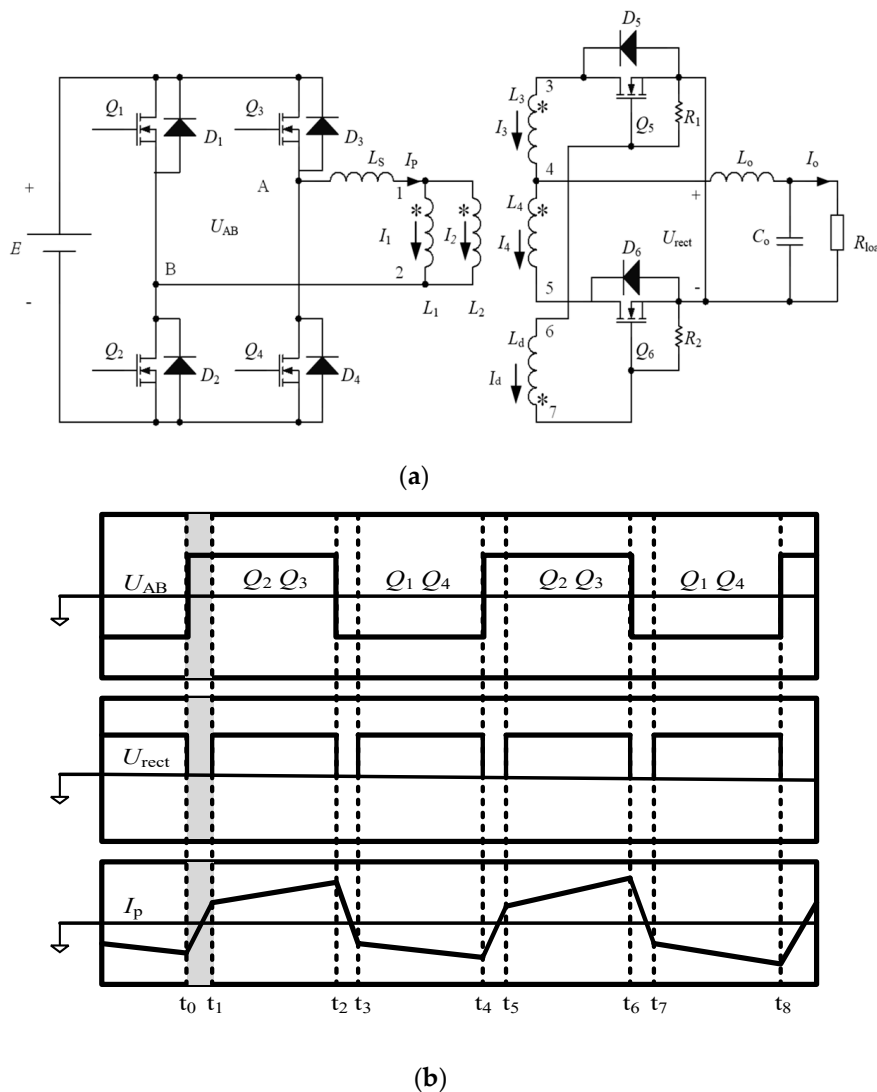


Figure 3. The proposed contactless bus converter. (a) Main circuit. (b) Key waveforms.

For the convenience of analysis, the influence of dead time is ignored. Main states of the circuit are shown in Figure 3b.

Before  $t_0$ ,  $Q_1$  and  $Q_4$  turn on and  $Q_2$  and  $Q_3$  turn off.  $U_{AB}$  is negative and imposed on the  $L_1$ ,  $L_2$ , and  $L_s$ . The currents on the transmitting coils decrease linearly to the negative maximum value. The coil  $L_d$  provides the driving signal for  $Q_5$ .

### 2.1.1. Mode I ( $t_0, t_1$ )

In this mode,  $Q_2$  and  $Q_3$  turn on and  $Q_1$  and  $Q_4$  turn off.  $U_{AB}$  voltage is positive. Since the transmitting current is less than the load current, the load current in the receiving side flows through  $D_5$  and  $D_6$  at the same time. As a result, the coils of from  $L_1$  to  $L_4$  are shorted, the  $U_{AB}$  voltage is imposed on  $L_s$  only, and the current increases rapidly in this mode. Since the input power does not transfer to the receiving side, the loss of the duty cycle appears in this mode. Obviously, a high coupling coefficient can reduce  $L_s$  and alleviate the impact of the loss of the duty cycle.

### 2.1.2. Mode II ( $t_1, t_2$ )

At  $t_1$ , the transmitting current  $I_1$  reaches the output current value.  $U_{AB}$  appears across  $L_1$ ,  $L_2$ , and  $L_s$ , and the power transfers to the receiving side again in this mode. The drive coil  $L_d$  provides the driving signal for  $Q_6$ . The current increases continuously.

After  $t_2$ ,  $Q_1$  and  $Q_4$  turn on and  $Q_2$  and  $Q_3$  turn off; the next half-cycle repeats.

## 2.2. Coil Structure

As mentioned before, we need to investigate the arrangement of double coils in pads for achieving full-wave synchronous rectification (FWSR). The transmitting pad consists of an inner coil and an outer coil, which are connected in parallel from terminals 1 and 2, as shown in Figure 4a. This coil arrangement can use the plane area fully and reduce the current flowing through a single coil. Therefore, the output power and efficiency can be improved. The receiving pad also contains inner and outer coils, as shown in Figure 3b. The inner coil is in serial with the outer coil to form a center-tapped structure. Three terminals: 3, 4, and 5 are used to achieve a full-wave self-synchronous rectification circuit. Actually, the coil arrangements in Figure 4a,b have a similar structure. The symmetrical structures in the space position can form a symmetrical coupling relationship easily. As a result, a balance-induced voltage in each half-switching period can be obtained. At the same time, the loss of the duty cycle also can be alleviated, since the double-coil structure can enhance the coupling coefficient.

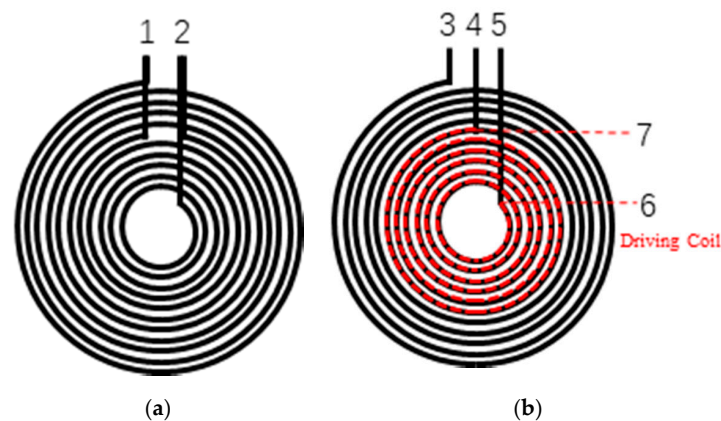


**Figure 4.** Coil arrangements on the power pads. (a) Transmitting side. (b) Receiving and driving side.

The red dotted line attached on the receiving coils in Figure 4b is the driving coil to generate a driving signal. Terminals 6 and 7 are connected to the gates of  $Q_5$  and  $Q_6$ , as shown in Figure 3a.

### 2.3. Equivalent Model

Coils  $L_3$  and  $L_4$  transfer the power to the load alternately. Since the working principles of  $L_3$  and  $L_4$  are the same, we take  $L_3$  as an example. When  $Q_1$ ,  $Q_4$ , and  $Q_5$  turn on, the equivalent circuit is shown in Figure 5.  $R_{L1}$ ,  $R_{L2}$ , and  $R_{L3}$  are the equivalent resistances of coils  $L_1$ ,  $L_2$ , and  $L_3$ , respectively.  $I_1$ ,  $I_2$ , and  $I_3$  are the RMS (root mean square) current flowing through coils  $L_1$ ,  $L_2$ , and  $L_3$ , respectively.  $M_{12}$ ,  $M_{13}$ , and  $M_{23}$  are the mutual inductance among the three coils, respectively.  $R_L$  is the load.

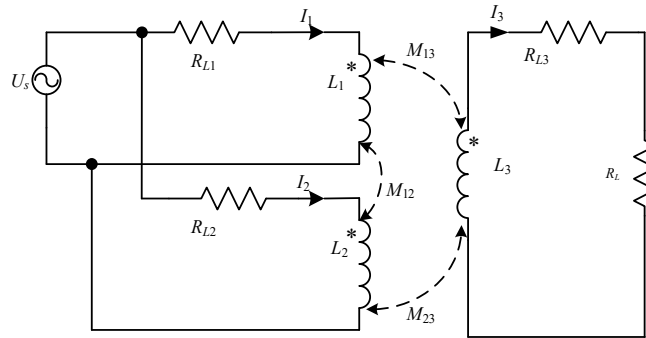


Figure 5. The equivalent circuit of the proposed structure.

The matrix equation of the system can be established

$$\begin{bmatrix} \dot{U}_s \\ \dot{U}_s \\ 0 \end{bmatrix} = \begin{bmatrix} Z_1 & j\omega M_{12} & -j\omega M_{13} \\ j\omega M_{12} & Z_2 & -j\omega M_{23} \\ -j\omega M_{13} & -j\omega M_{23} & Z_3 \end{bmatrix} \begin{bmatrix} \dot{I}_1 \\ \dot{I}_2 \\ \dot{I}_3 \end{bmatrix} \quad (1)$$

where  $Z_1$ ,  $Z_2$ , and  $Z_3$  are

$$\begin{cases} Z_1 = Z_{11} + \frac{\omega^2 M_{12}^2}{Z_{22}} + \frac{\omega^2 M_{13}^2}{Z_{33}} \\ Z_2 = Z_{22} + \frac{\omega^2 M_{12}^2}{Z_{11}} + \frac{\omega^2 M_{23}^2}{Z_{33}} \\ Z_3 = R_{L3} + j\omega L_3 + R_L \end{cases}$$

$Z_{11}$ ,  $Z_{22}$ , and  $Z_{33}$  are the impedance in the three coils, respectively, and  $L_1$ ,  $L_2$ , and  $L_3$  are the inductance of the coils, respectively.

$$\begin{cases} Z_{11} = R_{L1} + j\omega L_1 \\ Z_{22} = R_{L2} + j\omega L_2 \\ Z_{33} = R_{L3} + j\omega L_3 + R_L \end{cases}$$

The RMS values of  $I_1$ ,  $I_2$ , and  $I_3$  can be calculated from Equation (1):

$$\begin{cases} \dot{I}_1 = \frac{\dot{U}_s}{Z_1} = \frac{\dot{U}_s}{Z_{11} + \frac{\omega^2 M_{12}^2}{Z_{22}} + \frac{\omega^2 M_{13}^2}{Z_{33}}} \\ \dot{I}_2 = \frac{\dot{U}_s}{Z_2} = \frac{\dot{U}_s}{Z_{22} + \frac{\omega^2 M_{12}^2}{Z_{11}} + \frac{\omega^2 M_{23}^2}{Z_{33}}} \\ \dot{I}_3 = \frac{\dot{U}_s}{Z_3} = \frac{j\omega M_{13} \dot{I}_1 + j\omega M_{23} \dot{I}_2}{Z_{33}} \end{cases} \quad (2)$$

Based on Equation (2), the induced voltage  $U_3$  on  $L_3$  is

$$\dot{U}_3 = \dot{I}_3 R_L = \frac{j\omega M_{13} \dot{U}_s Z_{22} R_L}{Z_{11} Z_{22} Z_{33} + \omega^2 M_{12}^2 Z_{33} + \omega^2 M_{13}^2 Z_{22}} + \frac{j\omega M_{23} \dot{U}_s Z_{11} R_L}{Z_{11} Z_{22} Z_{33} + \omega^2 M_{12}^2 Z_{33} + \omega^2 M_{23}^2 Z_{11}} \quad (3)$$

Similarly, when  $Q_2, Q_3,$  and  $Q_6$  turn on, the induced voltage  $U_4$  on  $L_4$  is

$$\dot{U}_4 = \dot{I}_4 R_L = \frac{j\omega M_{14} \dot{U}_s Z_{22} R_L}{Z_{11} Z_{22} Z_{33} + \omega^2 M_{12}^2 Z_{33} + \omega^2 M_{13}^2 Z_{22}} + \frac{j\omega M_{24} \dot{U}_s Z_{11} R_L}{Z_{11} Z_{22} Z_{33} + \omega^2 M_{12}^2 Z_{33} + \omega^2 M_{23}^2 Z_{11}} \quad (4)$$

According to Equations (3) and (4),  $U_3$  and  $U_4$  are determined by many factors, such as self-inductance, mutual inductance, coil impedance, and load conditions. Therefore, optimizing coupling relationships between two pads is the key to reducing the induced voltage differences between  $U_3$  and  $U_4$ .

### 3. Optimal Structure of the Coils

#### 3.1. Relationship between the Induced Voltage and the Number of Turns

As mentioned before, the pads on both sides have the similar inner and outer structures with double coils. Since the outer coil has a larger diameter than the inner coil, the inductance of  $L_3$  will be greater than  $L_4$  if the turns of the two coils are the same. In this condition, the induced voltage from  $L_3$  and  $L_4$  in each half of the switching period will be unbalanced. Therefore, we need to optimize the turns of the inner and outer coils to get a similar induced voltage.

The self-inductance of a planar coil is determined by the shapes, turns, and sizes.  $R_{3min}, R_{4min}, R_{3avg}, R_{4avg}, R_{3max}$  and  $R_{4max}$  are the minimum radius, average radius, and maximum radius of  $L_3$  and  $L_4$ , respectively, as shown in Figure 6a. The individual self-inductance of planar coils  $L$  can be calculated roughly based on Equation (5) [24].

$$L = 2.15 \times 10^{-6} R_{avg} N^{\frac{5}{3}} \ln\left(\frac{8R_{avg}}{R_{max} - R_{min}}\right) \quad (5)$$

where  $N$  is the turns of coil  $L$ .

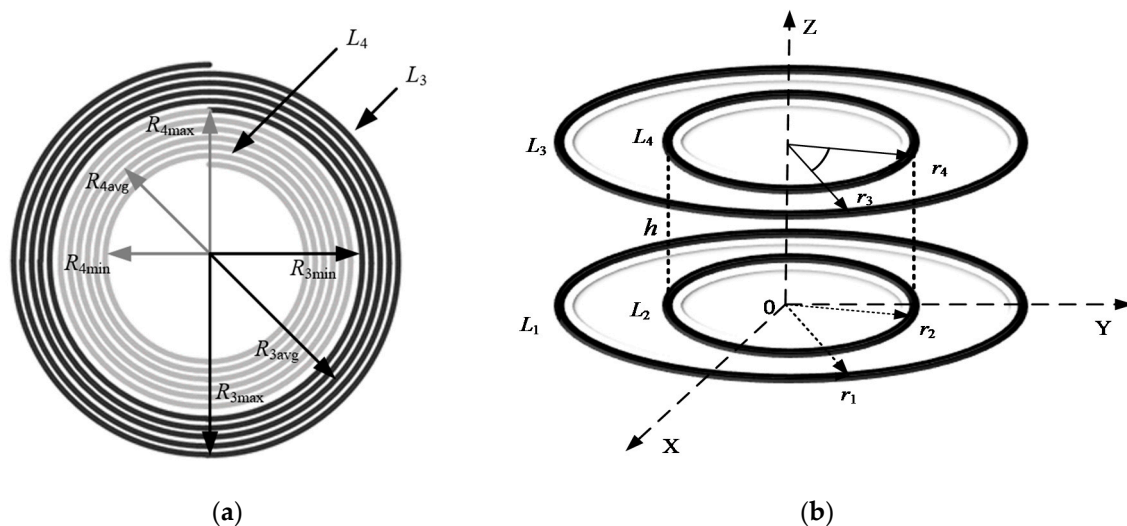


Figure 6. Parameter with coils. (a) Coil structures. (b) Space positions in the proposed structure.

Figure 6b shows the space positions of four coils in the transmitting pad and the receiving pad. In order to analyze the mutual inductance between the four coils, we set the radius of coils  $L_1, L_2, L_3,$  and  $L_4$  as  $r_1, r_2, r_3,$  and  $r_4$ , respectively. The space positions of coils  $L_1$  and  $L_2$  in the X-Y plane are the same with coils  $L_3$  and  $L_4$ , and the distance between two pads is  $h$ .

According to Neumann’s formula, the mutual inductance between two coils can be expressed as Equation (6):

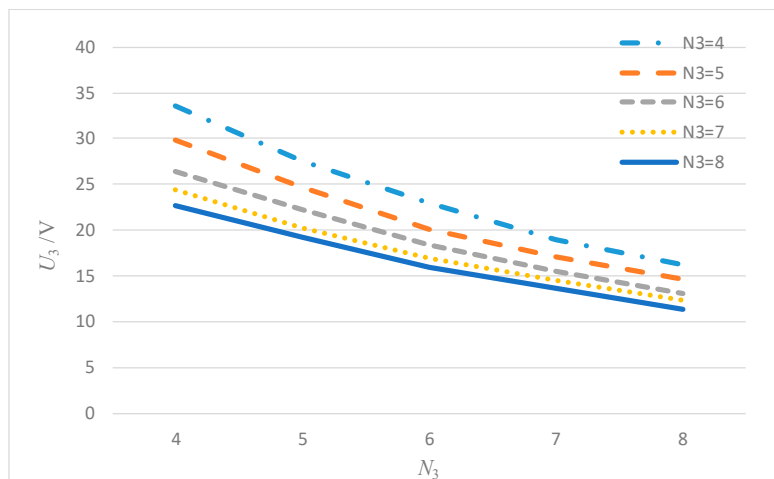
$$M_{L_a, L_b} = \mu_0 \sqrt{r_a r_b} \left[ \left( \frac{2}{k} - k \right) K(k) - \frac{2}{k} E(k) \right] \quad (6)$$

where  $k = \sqrt{4r_a r_b / [(r_a + r_b)^2 + h^2]}$ .  $K(k)$  and  $E(k)$  are complete elliptic integrals of the first and second kind, respectively [25].

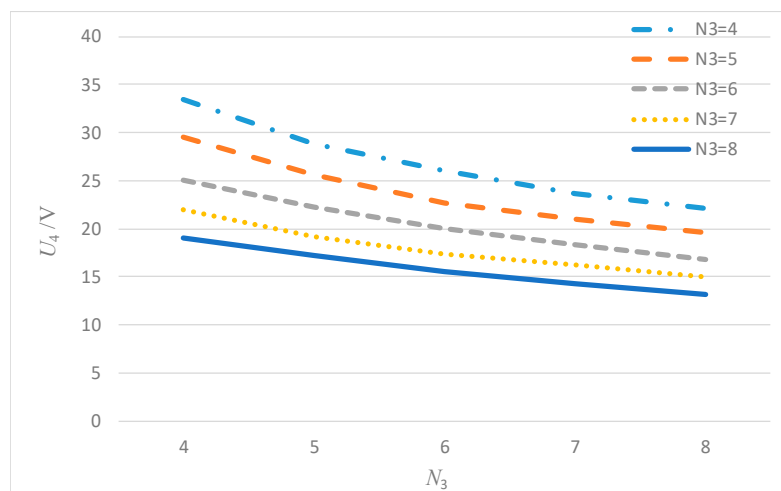
As shown in Figure 6, the turns of coils  $L_1$ ,  $L_2$ ,  $L_3$ , and  $L_4$  are  $N_1$ ,  $N_2$ ,  $N_3$ , and  $N_4$ , respectively, and  $N_1=N_3$  and  $N_2=N_4$  here. Then, the mutual inductance between  $L_1$  and  $L_3$  can be calculated roughly based on Equation (7).

$$M_{L_1, L_3} = \sum_{i=1}^{N_1} \sum_{j=1}^{N_3} M_{L_1, N_1=i, L_3, N_3=j} \quad (7)$$

Based on Equations (6) and (7), the mutual inductance relates to the turns and diameters of the coils. Therefore, the relationship of mutual inductance between coils can be adjusted by selecting the turns of the coils. In order to evaluate the effect of coils with different turn ratio on the induced voltage, Ansys Maxwell 2017 software is used to analyze the results under different configurations. The outer diameter of the coil is 75 mm, the air gap distance is 2 mm, the input voltage is 30 V, the switching frequency is 100 kHz, and the load is 3 ohm. Extracting the relative parameters of Equations (3) and (4) based on the Maxwell software, the relationships between  $N_3$ ,  $N_4$ ,  $U_3$ , and  $U_4$  can be obtained, as shown in Figure 7.



(a)



(b)

**Figure 7.** Induced voltages at the power-receiving coils under different turn ratios. (a)  $U_3$  in the coil  $L_3$ . (b)  $U_4$  in the coil  $L_4$ .

The relationships among  $U_3$ ,  $N_3$ , and  $N_4$  are shown in Figure 7a. When  $N_4$  is fixed,  $U_3$  decreases with the increasing  $N_3$ . When  $N_3$  is fixed,  $U_3$  decreases with the increasing  $N_4$ . The relationships among  $U_4$ ,  $N_3$ , and  $N_4$  are shown in Figure 7b. Similarly, when  $N_3$  is fixed,  $U_4$  decreases with the increasing  $N_4$ . When  $N_4$  is fixed,  $U_4$  decreases with the increasing  $N_3$ .

It also can be observed from Figure 7 that the effects of different combinations of  $N_3$  and  $N_4$  on  $U_3$  and  $U_4$  are different. The induced voltage  $U_3$  at the outer coil is more sensitive to those different combinations. Therefore, we need to configure the turns of  $N_3$  and  $N_4$  to obtain a balanced induced voltage.

Assuming that voltage  $U_{\text{error}}$  is the difference between  $U_3$  and  $U_4$ , as Equation (8):

$$U_{\text{error}} = |U_3 - U_4| \quad (8)$$

In order to get a similar induced voltage in each half of the switching period, the differences between  $U_3$  and  $U_4$  should be minimized. Based on Figure 7 and Equation (8), Figure 8 shows three combinations where  $U_{\text{error}}$  has the minimum values—that is,  $N_3 = 4$  and  $N_4 = 4$ ,  $N_3 = 5$  and  $N_4 = 6$ , and  $N_3 = 6$  and  $N_4 = 8$ . The numbers of  $N_3$  and  $N_4$  determine the values of the output voltage also, so  $N_3 = 5$  and  $N_4 = 6$  are used in our design.

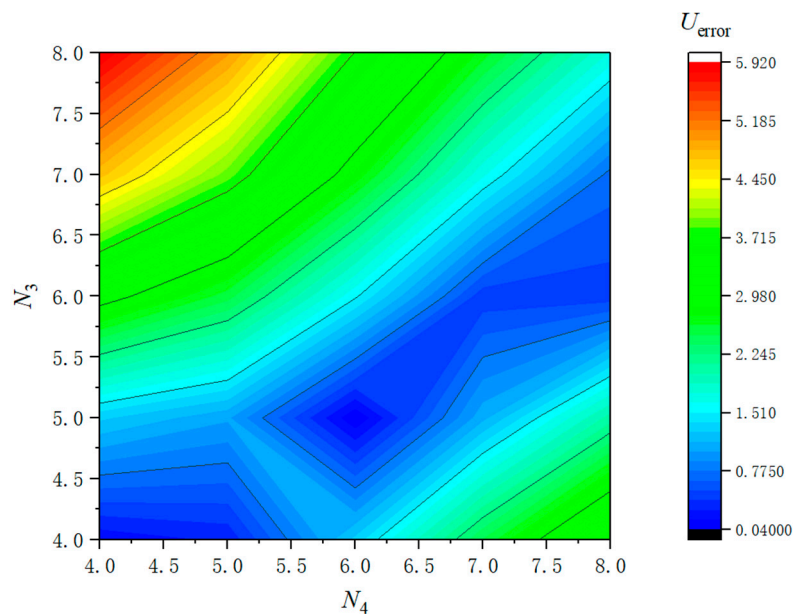


Figure 8. The relationships among  $N_3$ ,  $N_4$ , and  $U_{\text{error}}$ .

### 3.2. Driving Coil Arrangement

Figure 9 shows the equivalent circuits of the driving blocks [26]. Since both coils  $L_1$  and  $L_2$  have the coupling relationships with the driving  $L_d$ , the induced voltage  $V_B$  across  $L_d$  is composed of two equivalent voltage sources. The equivalent leakage inductance is  $L_t$ , the equivalent coil resistance is  $R_S$ , the gate capacitance of the switch is  $C_g$ , and the resistance  $R_P$  is in parallel with  $C_g$ .

The circuit of Figure 9 follows Equation (9):

$$U_c(t) = V_B \cdot \frac{R_P}{R_P + R_S} \cdot \left[ 1 - \frac{e^{-\zeta \omega_n t}}{\sqrt{1 - \zeta^2}} \sin(\omega_d t) \right] \quad (9)$$

where

$$\zeta = \frac{1}{2} \left( \frac{1}{C_g R_P} + \frac{R_S}{L_t} \right) \sqrt{\frac{L_t C_g R_P}{R_S + R_P}}$$

$$\omega_n^2 = \frac{R_S + R_P}{L_t C_g R_P}$$

$$\omega_\delta = \omega_n \sqrt{1 - \zeta^2}$$

$$V_B = \omega M_{1d} I_1 + \omega M_{2d} I_2$$

In order to achieve a balance between the rapid response and small voltage spike, the driving circuit should work under an underdamped state with a rapid attenuation. The damping constant  $\zeta \cdot \omega_n$  is

$$\zeta \cdot \omega_n = \frac{1}{2} \left( \frac{1}{C_g \cdot R_P} + \frac{R_S}{L_t} \right) \tag{10}$$

$C_g$  is determined by the parasitic capacitance of switches.  $R_S$  and  $R_P$  are associated with the driving speed and resistance losses, respectively. Therefore, for a loose coupling system, we should minimize the leakage inductance  $L_t$  between the transmitting coils and the driving coils. The steady-state induced voltage  $V_B$  can be controlled by selecting suitable turns of the driving coils.

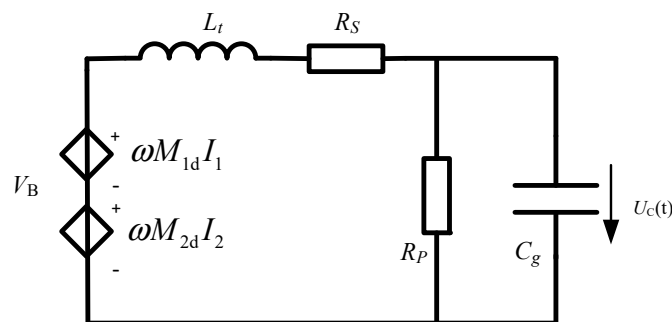


Figure 9. Equivalent circuits of the driving blocks.

From Equation (10), a large leakage inductance  $L_t$  may lead to a serious oscillation in the driving voltage waveforms. Four typical arrangements of the driving coils are compared, such as loose outer, tight outer, loose inner, and tight inner, as shown in blue lines in Figure 10a–d, respectively. The mutual inductance between  $L_1$  and  $L_d$  is  $M_{1d} = \sqrt{L_1 L_d} \cdot k_{1d}$ , and the mutual inductance between  $L_2$  and  $L_d$  is  $M_{2d} = \sqrt{L_2 L_d} \cdot k_{2d}$ . Therefore, the total mutual inductance  $M_S$  between the transmitting double coils and the driving coil is

$$M_S = M_{1d} + M_{2d} \tag{11}$$

Using Maxwell software, we simulate the values of  $M_{1d}$ ,  $M_{2d}$ ,  $L_1$ , and  $L_d$ . Based on Equation (11) and the simulated data, Figure 11 shows the total mutual inductance  $M_S$  under four typical arrangement coils. When the coil is in the loose outer arrangement,  $M_S$  has the largest value.  $M_S$  has the lowest value when the driving coil is in the arrangement of tight inner.

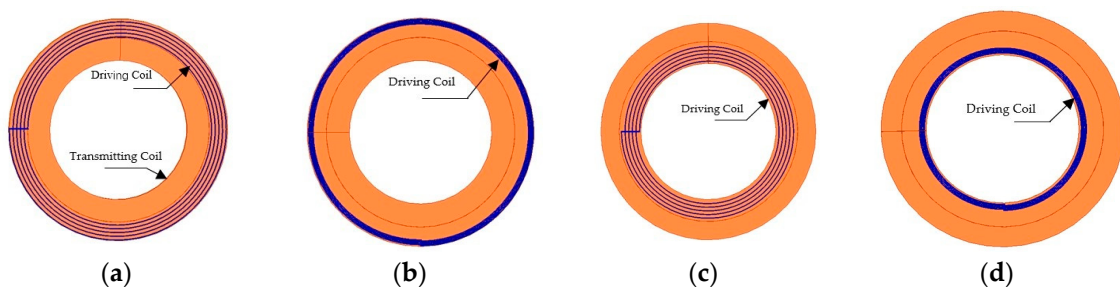
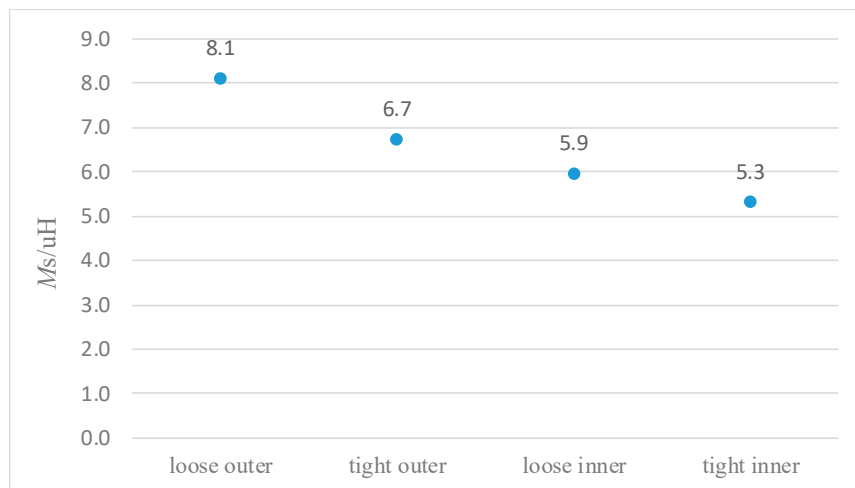


Figure 10. Typical arrangements of the driving coil: (a) loose outer, (b) tight outer, (c) loose inner, and (d) tight inner.



**Figure 11.** The mutual inductance of the driving coil under four typical arrangements.

#### 4. Loss of Duty Cycle Analysis

In the loosely coupled contactless power transfer system, leakage inductance will cause the loss of the duty cycle, which greatly reduces the power transfer and the output voltage. The duty cycle loss  $D_{loss}$  is defined as the differences between the duty cycle  $D_p$  at the transmitting side and  $D_s$  at the receiving side, as shown in the shaded part in Figure 2b. Therefore, the loss of the duty cycle also can be defined as the ratio between  $t_{01}$  and  $T_s/2$  [27].

$$D_{loss} = D_p - D_s = \frac{t_{01}}{T_s/2} \propto \frac{L_s I_o}{V_{in}} \quad (12)$$

From Equation (12), the average output current  $I_o$  and leakage inductance  $L_s$  play a direct role on the  $D_{loss}$ . Since  $I_o$  is determined by the requirements of the maximum loads, we should minimize the leakage inductance,  $L_s$ .

From Figure 5, power-transmitting coils  $L_1$  and  $L_2$  are coupled with power-receiving coil  $L_3$  at the same time. The coupling coefficient  $k_{13}$  is the coupling relationships between  $L_1$  and  $L_3$ , and  $k_{23}$  is the coupling relationships between  $L_2$  and  $L_3$ . We take  $k_{13}$  as a variable and use Maxwell software to analyze the relationship among the coupling coefficient  $k$ , load current, and  $D_{loss}$ , as shown in Figure 12. It shows that a higher coupling coefficient will reduce the sensitivity of  $D_{loss}$  to the load current.

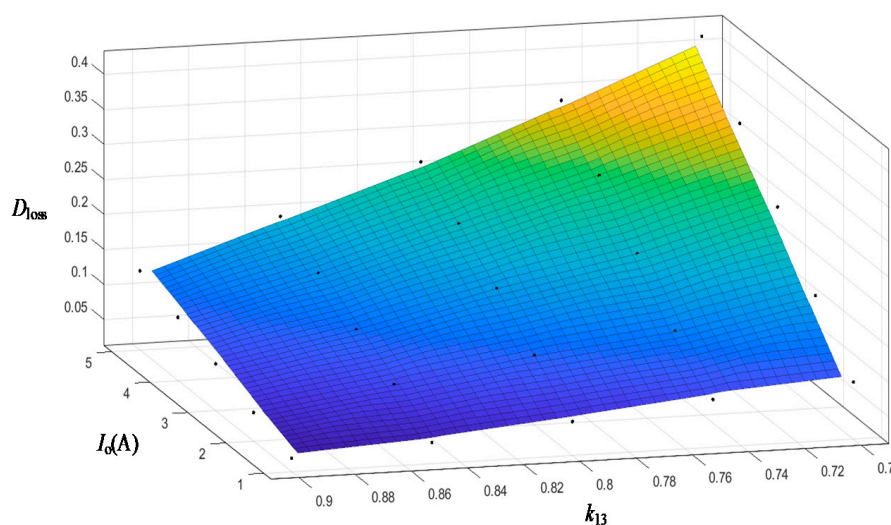


**Figure 12.** Relationships among  $k_{13}$ , the load currents, and  $D_{loss}$ .

### 5. Experimental Verification

A 120 W experimental platform was built to verify the proposed method, as shown in Figure 13. The power transmitting coils, receiving coils, and driving coil are shown in Figure 14. The key experimental parameters are listed in Table 1.

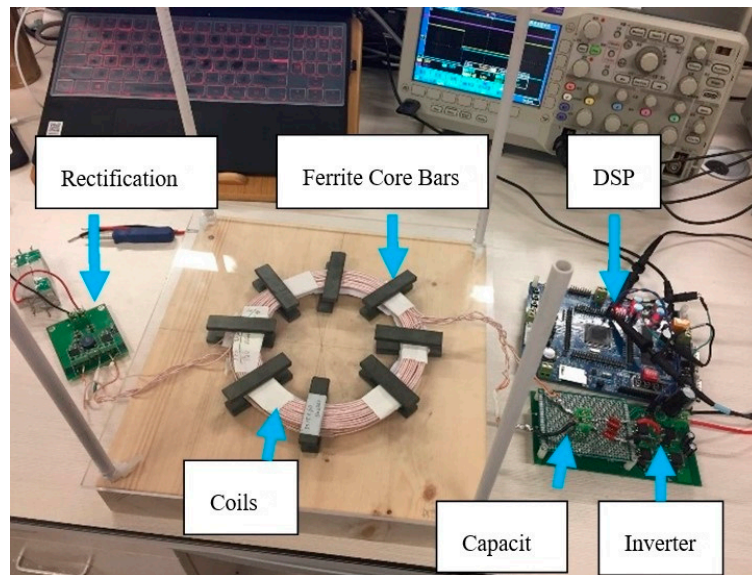


Figure 13. Experimental platform.

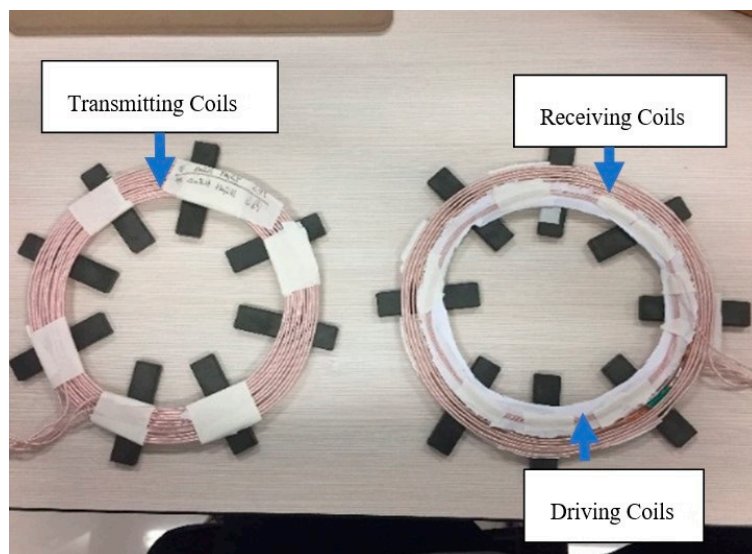


Figure 14. Structures of the power coils.

Table 1. Experimental parameters of the system.

Parameters	Value
$L_1, L_3/\mu\text{H}$	21.8( $N_1 = 5$ )
$L_2, L_4/\mu\text{H}$	22.5( $N_2 = 6$ )
Air gap distance/mm	2
Coil diameter /mm	75
Input Voltages $U_s/\text{V}$	30
Frequency $f/\text{kHz}$	100
Ferrite core bars	PC40 (5 × 15 × 60 mm)
Litz wire	300 strands × 0.1 mm

Figure 15 shows the induced voltage waveforms in the outer coil  $L_3$  and the inner coil in  $L_4$ , respectively. It can be observed that the amplitudes of the induced voltage of  $L_3$  and  $L_4$  are almost the same. Therefore, using Equations (3), (4), and (10) to optimize turn ratio of the coils can reduce the differences of the induced voltage effectively.

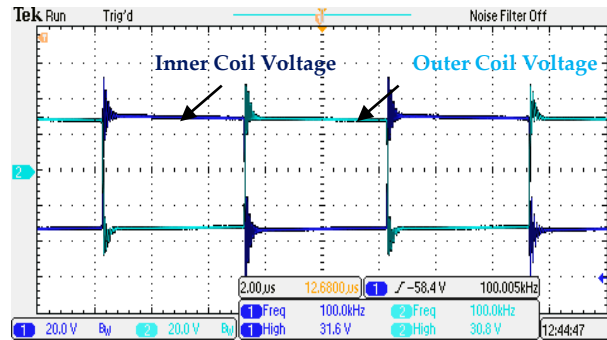


Figure 15. Inductive voltage waveform from the inner and outer double coils on the receiving side.

To a driving coil circuit, we need to consider the amplitudes of the driving voltage, oscillation spikes, and difficult aspects in fabrication. The voltage waveforms of the driving coil under four typical arrangements are shown in Figure 16. As the analysis results of the mutual inductance in Figure 11, Figure 16a shows that the induced voltage in the loose outer is 15 V, which is higher than those arrangements under the tight outer (14.6 V), loose inner (13 V), and tight inner (12.6 V), as shown in Figure 16b–d.

Benefiting from the relatively low leakage inductance, the oscillation of the driving voltage spike in loose coils is smaller than in tight coils from Figure 16a–d. This phenomenon can be explained by Equation (9)—that the peak voltage in the driving signal is associated with the leakage inductor. Therefore, the loose coil arrangements show a better performance for the driving circuit.

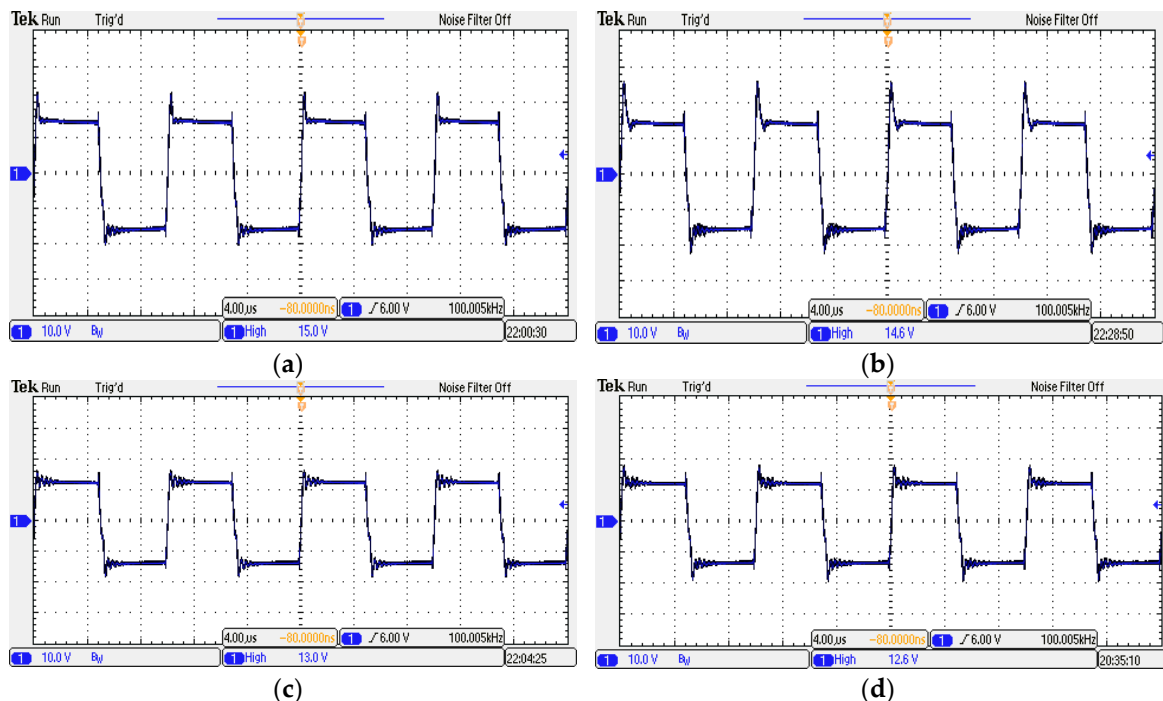


Figure 16. Driving waveforms of four typical coil layouts: (a) loose outer, (b) tight outer, (c) loose inner, and (d) tight inner.

We tested the proposed structure without ferrite core bars first. When the output current was 6 A, the duty cycle was 40% only, and the loss of the duty cycle was 10%, as shown in Figure 17. The output voltage was only 18.5 V at 6 A, and the efficiency of system was 86.5%.

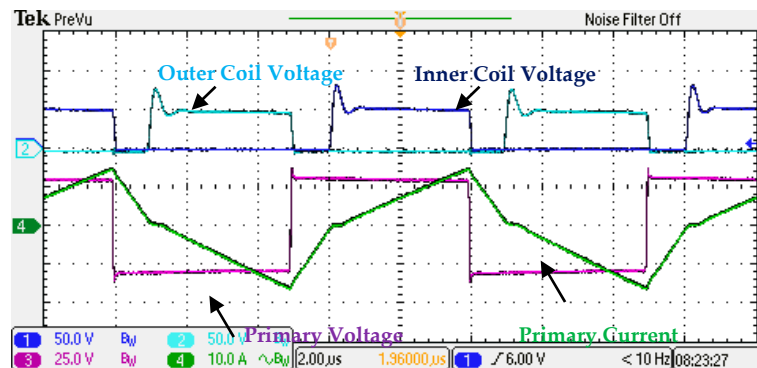


Figure 17. Current and voltage waveforms under the 6 A load current without ferrite core bars.

For a given system, using ferrite bars can improve the efficiency but also add weight. Therefore, we have to make a compromise between these two points. Especially when the custom system is very sensitive to weight, we have to select the minimum ferrite bars to meet the electrical requirements. Figure 18 shows the changing tendency of the output voltages with the increasing ferrite core bars. Obviously, more ferrite core bars will result in a higher output voltage. At the same time, the simulated results based on Maxwell software fit the experimental results very well. This shows that the key circuit parameters extracted from Maxwell software can be used for modeling systems correctly.

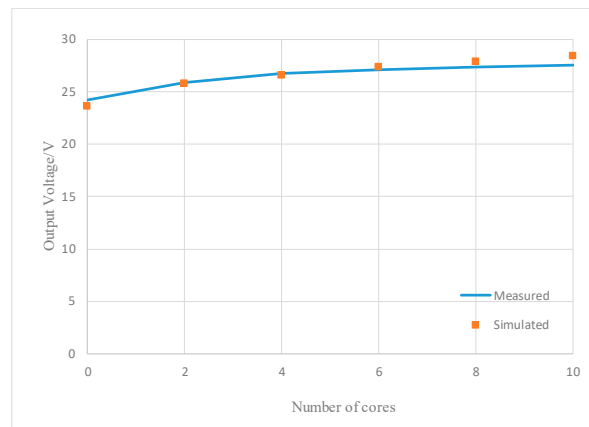
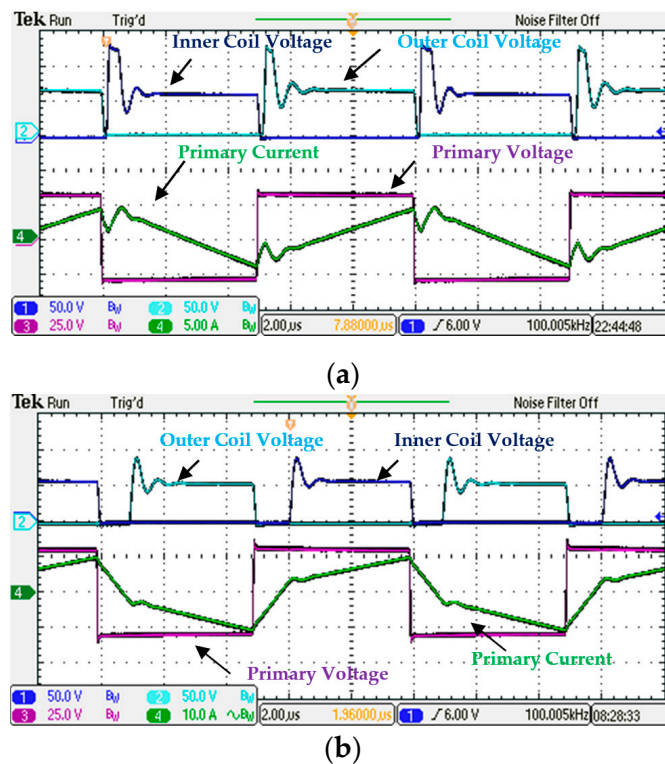


Figure 18. Comparison between simulated and measured output voltages with the increasing ferrite core bars.

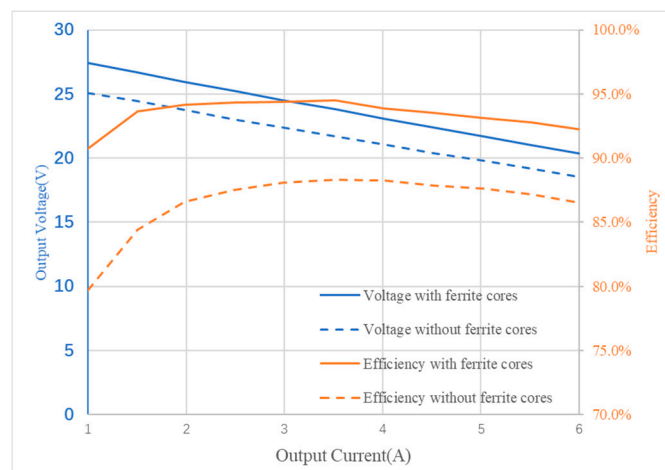
In order to enhance the efficiency and load regulation ratio, eight ferrite core bars on each pad have been added, as shown in Figure 14. The key waveforms under the output current of 1 A and 6 A are shown in Figure 19a,b, respectively. In Figure 19a, under the 1 A output current, the duty cycle in the power-receiving side is 48.80%, and the loss of the duty cycle is 1.2%, roughly.

Figure 19b shows the key waveforms under the 6A output currents. The loss of the duty cycle is 9.43%. The output voltage is 20.3 V, and the efficiency of the system is 92.2% under 6 A. Compared with the experimental results in Figure 17, the efficiency is improved 5.7% under 6 A, with eight ferrite core bars. At the same time, the output power is also increased to 10.8 W, which benefits from the higher output voltage.



**Figure 19.** Current and voltage waveforms with 8 ferrite core bars: (a) under the 1 A load current and (b) under the 6 A load current.

Figure 20 shows the experimental results of the output current, output voltage, and efficiency with and without the ferrite cores, respectively. With the ferrite core bars, the efficiency of the system reaches 90.7% under all load conditions, and the peak efficiency is 94.5% at 3.5 A.



**Figure 20.** Relationships among the efficiencies, load currents, and voltages.

## 6. Conclusions

This paper shows the architecture of an unregulated contactless power converter, which can provide a solution for a separable modular design. The proposed structure can enhance the ability of the power transfer between two pads and improve the efficiency. In order to get a balance-induced voltage in each half of the switching period, the turns of the inner coil and the outer coil are optimized. Full-wave synchronous rectification is used for meeting the requirements of the applications of low output voltage with high output current.

The structures of the self-driven coils are discussed to provide stable driving signals. Four typical arrangements of driving coils are analyzed in detail. The structures of the driving coils can be selected based on the voltage levels, the convenience of production, and cost. The coupling coefficient of the system can be increased by adding magnetic core bars, which can reduce the loss of the duty cycle and load regulation ratio. Therefore, in practice, the magnetic cores and the turns of the coils can be selected according to the design requirements of the weight and coil size. A 120-W unregulated intermediate bus converter prototype was built and achieved an efficiency of 90.7% under all loading ranges. The self-driven synchronous signal retention technology in a dead zone can further improve the efficiency of the system, which can enhance the efficiency further in the future.

**Author Contributions:** Methodology, Y.S. and Y.Z.; Software, Z.Y.; Supervision, Y.Z.; Validation, Y.S.; Writing—original draft, Y.S.; Writing—review & editing, Y.Z. All authors have read and agreed to the published version of the manuscript.

**Funding:** This work is supported by the National Natural Science Foundation of China (51777098), Jiangsu Natural Science Foundation (SBK2019021122), Green and Blue Project in Jiangsu Province, Jiangsu Province Graduate Research and Practice Innovation Plan (SJCX19\_0260), and the Jiangsu Province Graduate Research and Practice Innovation Plan (SJCX19\_0261).

**Conflicts of Interest:** The authors declare no conflict of interest.

## Nomenclature

$VD_1 \sim VD_4$	diodes
$L_1 \sim L_4$	power transmitting and receiving coils
$L_d$	driving coil
$L_o$	output filter inductor
$L_s$	leakage inductance on primary side
$I_1 \sim I_4$	current in $L_1, L_2, L_3, L_4$ , respectively
$I_p$	current on leakage inductance
$I_d$	current on driving coil
$D_1 \sim D_6$	diodes
$Q_1 \sim Q_6$	power MOSFET
$R_1, R_2$	gate resistance of power MOSFET
$R_{load}$	Load resistance
$U_{AB}$	Inverter output
$U_{rect}$	rectification voltage
$C_o$	output filter capacitor
$E$	DC power supply
$N_1 \sim N_4$	turn ratio of coils of $L_1, L_2, L_3, L_4$ , respectively
$M_{12}, M_{13}, M_{14}, M_{23}, M_{24}, M_{34}$	mutual inductance between coils of $L_1, L_2, L_3, L_4$ , respectively
DSP	Digital Signal Processor

## References

1. Thenathayalan, D.; Park, J.H. Wide-Air-Gap transformer model for the design-oriented analysis of contactless power converters. *IEEE Trans. Ind. Electron.* **2015**, *62*, 6345–6359. [[CrossRef](#)]
2. Sibué, J.-R.; Kwimang, G.; Ferrieux, J.P.; Meunier, G.; Roudet, J.; Périot, R. A global study of a contactless energy transfer system: Analytical design, virtual prototyping, and experimental validation. *IEEE Trans. Power Electron.* **2012**, *28*, 4690–4699. [[CrossRef](#)]
3. Yang, Q.; Lin, B.; Luan, Y.; Duan, J. Distributed capacitance effects on the transmission performance of contactless power transfer for rotary ultrasonic grinding. *IET Power Electron.* **2018**, *11*, 548–556. [[CrossRef](#)]
4. Matsumoto, H.; Shibako, Y.; Neba, Y. Contactless power transfer system for AGVs. *IEEE Trans. Ind. Electron.* **2018**, *65*, 251–260. [[CrossRef](#)]
5. He, G.; Chen, Q.; Ren, X.; Wong, S.C.; Zhang, Z. Modeling and design of contactless sliprings for rotary applications. *IEEE Trans. Ind. Electron.* **2019**, *66*, 4130–4140. [[CrossRef](#)]
6. Covic, G.A.; Boys, J.T. Inductive power transfer. *Proc. IEEE.* **2013**, *101*, 1276–1289. [[CrossRef](#)]

7. Covic, G.A.; Boys, J.T. Modern trends in inductive power transfer for transportation applications. *IEEE J. Emerg. Sel. Top. Power Electron.* **2013**, *1*, 28–41. [CrossRef]
8. Low, Z.N.; Chinga, R.A.; Tseng, R.; Lin, J. Design and test of a high-power high-efficiency loosely coupled planar wireless power transfer system. *IEEE Trans. Ind. Electron.* **2008**, *56*, 1801–1812. [CrossRef]
9. Jow, U.-M.; Ghovanloo, M. Geometrical design of a scalable overlapping planar spiral coil array to generate a homogeneous magnetic field. *IEEE Trans. Magn.* **2013**, *49*, 2933–2945. [CrossRef]
10. Miwa, K.; Mori, H.; Kikuma, N.; Hirayama, H.; Sakakibara, K. A consideration of efficiency improvement of transmitting coil array in wireless power transfer with magnetically coupled resonance. In Proceedings of the 2013 IEEE Wireless Power Transfer (WPT), Perugia, Italy, 15–16 May 2013; pp. 13–16.
11. Santalunai, S.; Thongsopa, C.; Thosdeekoraphat, T. An increasing the power transmission efficiency of flat spiral coils by using ferrite materials for wireless power transfer applications. In Proceedings of the 2014 11th International Conference on Electrical Engineering/Electronics, Computer, Telecommunications and Information Technology (ECTI-CON), Nakhon Ratchasima, Thailand, 14–17 May 2014; pp. 1–4.
12. Liu, X.; Hui, S.Y. Optimal design of a hybrid winding structure for planar contactless battery charging platform. *IEEE Trans. Power Electron.* **2008**, *23*, 455–463. [CrossRef]
13. Lu, F.; Zhang, H.; Hofmann, H.; Mi, C.C. An inductive and capacitive combined wireless power transfer system with LC-compensated topology. *IEEE Trans. Power Electron.* **2016**, *31*, 8471–8482. [CrossRef]
14. Baek, J.-I.; Kim, C.-E.; Lee, J.-B.; Youn, H.-S.; Moon, G.-W. A simple SR gate driving circuit with reduced gate driving loss for phase-shifted full-bridge converter. *IEEE Trans. Power Electron.* **2018**, *33*, 9310–9317. [CrossRef]
15. TEA1761 Datasheet. Available online: <https://www.nxp.com/docs/en/data-sheet/TEA1761T.pdf> (accessed on 25 April 2007).
16. Fernández, A.; Carbonnier, H.; Mourra, O.; Tonicello, F. 28V bus solar array regulator based on converters with transformer and self-driven Synchronous Rectification. In Proceedings of the 2012 IEEE Energy Conversion Congress and Exposition (ECCE), Raleigh, NC, USA, 15–20 September 2012; pp. 1088–1094.
17. Qian, T.; Song, W.; Lehman, B. Self-driven synchronous rectification scheme for wide range application of DC/DC converters with symmetrically driven transformers. In Proceedings of the 2006 37th IEEE Power Electronics Specialists Conference, Jeju, Korea, 18–22 June 2006; pp. 1–6.
18. Zhong, W.X.; Hui, S.Y.; Ho, W.C.; Ho, W.C.; Liu, X. Using self-driven AC–DC synchronous rectifier as a direct replacement for traditional power diode rectifier. *IEEE Trans. Ind. Electron.* **2012**, *59*, 392–401. [CrossRef]
19. Tuomainen, V.; Kyyra, J. Effect of resonant transition on efficiency of forward converter with active clamp and self-driven SRs. *IEEE Trans. Power Electron.* **2005**, *20*, 315–323. [CrossRef]
20. Fernández, A.; Sebastian, J.; Alou, P.; Cobos, J.; Rascon, M. Low output voltage AC/DC converter with a new scheme of synchronous rectification that complies with IEC 1000-3-2 regulations. *IEEE Trans. Power Electron.* **2003**, *18*, 966–974. [CrossRef]
21. Gu, Y.; Lu, Z.; Qian, Z.; Huang, G. A novel driving scheme for synchronous rectifier suitable for modules in parallel. *IEEE Trans. Power Electron.* **2005**, *20*, 1287–1293. [CrossRef]
22. Guan, Y.; Wang, Y.; Bian, Q.; Hu, X.; Wang, W.; Xu, D. High-efficiency self-driven circuit with parallel branch for high frequency converters. *IEEE Trans. Power Electron.* **2018**, *33*, 926–931. [CrossRef]
23. Qian, T.; Song, W.; Lehman, B. Self-driven synchronous rectification scheme without undesired gate-voltage discharge for DC-DC converters with symmetrically driven transformers. *IEEE Trans. Power Electron.* **2008**, *23*, 506–510. [CrossRef]
24. Dill, H.G. Designing inductors for thin-film applications. *Electron. Des.* **1964**, *17*, 52–60.
25. Maxwell, J.C. *A Treatise on Electricity and Magnetism*; Dover: New York, NY, USA, 1954.
26. Alou, P.; Cobos, J.; Garcia, O.; Prieto, R.; Uceda, J. A new driving scheme for synchronous rectifiers: Single winding self-driven synchronous rectification. *IEEE Trans. Power Electron.* **2001**, *16*, 803–811. [CrossRef]
27. Wang, H.; Chung, H.S.-H.; Ioinovici, A. A class of high-input low-output voltage single-step converters with low voltage stress on the primary-side switches and high output current capacity. *IEEE Trans. Power Electron.* **2011**, *26*, 1659–1672. [CrossRef]

